D.A. Dei Tos, F. Topputo
High-Fidelity Trajectory Optimization with Application to Saddle-Point Transfers
Journal of Guidance Control and Dynamics, Vol. 42, N. 6, 2019, p. 1343-1352
doi:10.2514/1.G003838

High-Fidelity Trajectory Optimization with Application to Saddle Point Transfers

Diogene A. Dei Tos* and Francesco Topputo†
Politecnico di Milano, 20156 Milan, Italy

A method to optimize space trajectories subject to impulsive controls is presented. The method employs a high-fidelity model and a multiple shooting technique. The model accounts for an arbitrary number of gravitational attractions, their corrections due to celestial bodies oblateness, and solar radiation pressure. The peculiarity of this paradigm is that the equations of motion are written in a roto-pulsating frame, where two primaries are at rest despite the fact that their motion and the one of the perturbers is given by a real ephemeris model. Direct transcription of the dynamics coupled with a multiple shooting technique, and an efficient computation of the Jacobian of the defects are used to optimize trajectories subject to a finite number of impulsive controls. The method has been applied to find a multitude of solutions to the problem of transferring a spacecraft from the Sun–Earth collinear Lagrange points to the Sun–Earth gravitational saddle point, where a theoretical zero background acceleration allows testing possible deviations from General Relativity. The problem of targeting the Sun–Earth saddle point with high accuracy represents a major flight dynamics challenge. The applicative scenario encompasses the possible mission extension option for LISA Pathfinder as special case.

I. Introduction

The design of space missions is generally characterized by severe requirements on the Δv budget. Navigation is also becoming more and more challenging, asking for the satisfaction of stringent conditions characterized by unprecedented accuracy [1]. As a consequence, an increased complexity in the trajectory design is needed, ultimately leading to employing high-fidelity models already in the early stages of trajectory design [2]. Flying in highly nonlinear gravity fields allows exploiting unique features, such as libration point orbits (LPO) [3], ballistic captures [4], and low-energy transfers [5]. Beside generating unique orbits, multi-body models involve propellant savings, launch window widening, and overall safety increase [6, 7]. These features are achieved by exploiting the sensitivity in initial conditions of highly nonlinear environments, and open up new scenarios for spacecraft characterized by very limited thrust authority. Examples are interplanetary CubeSats, where incorporating the additional forces earlier in the design may be the key to success.

*PostDoc Research Fellow, Department of Aerospace Science and Technology; diogenealessandro.deitos@polimi.it.
†Assistant Professor, Department of Aerospace Science and Technology; francesco.topputo@polimi.it. Member AIAA.

Several aspects of high-fidelity modeling have been studied. The introduction of a novel solar system model in rotating coordinates [8] and a hierarchal approach have proven beneficial in numerical continuation processes [9]. The impact of a dynamical selection of primaries on the accuracy and computational cost of propagations is investigated in [10]. Efforts have been put into a fast, accurate, and smooth planetary ephemeris retrieval system [11]. Direct methods leveraging the full gravitational potential have proven effective for orbit design of ultra low thrust orbits [12].

In this work, a model that describes the motion of a massless particle subject to an arbitrary number of gravitational attractions, their corrections due to bodies oblateness, and solar radiation pressure is presented. The developed paradigm departs from standard Newtonian approach and builds a model that employs a roto-pulsating frame, where two primaries are at rest despite their true motion, which is given by ephemeris look-up tables. This model is ideal to refine preliminary solutions designed in restricted three- or four-body problems since these are described in rotating frames, convergence is smoother, a quicker geometrical interpretation of results is granted, and a hierarchical approach is leveraged [9]. The variational equations are also derived, from which the state transition matrix can be achieved. (A basic version of the roto-pulsating restricted n-body problem (RPRnBP) accounting for third bodies perturbations can be found in [2, 8, 9].)

The literature on space trajectory optimization with multiple shooting is vast, and thus the focus is only on those works where a rich dynamics is considered. Multiple shooting methods with propagation of the variational equations in n-body dynamics are used in [13, 14] for trajectory optimization, and in [15] to analyze the evolution of quasi-periodic orbits in the Earth–Moon system. Multiple shooting techniques are used to compute constrained transfers to LPO with a sequence of impulsive control maneuvers [16], as well as for the solution of low-thrust transfers in the Earth–Moon system, including applications to LPO [17]. Direct transcription of the dynamics is also employed in low-thrust trajectories to boost numerical efficiency [18]. Pseudo-spectral methods for optimal control have also shown promising results [19, 20]. In this work, a multiple-burn, multiple-shooting optimization is carried out in the RPRnBP. A transcription strategy that reduces interdependence among shooting arcs is formulated to ease solution convergence. A fast, efficient computation of the defects vector Jacobian is also implemented.

Motivated by the proposed mission extension of LISA Pathfinder, the application scenario deals with transfers from the Sun–Earth $L_{1,2}$ LPO to the Sun–Earth gravitational saddle point (SP). Unlike the Lagrange points where the gravitational potential has to cancel out the centrifugal acceleration, saddle points are regions of arbitrarily small gravitational force residing in a finite domain of very small extent. They are, therefore, ideal locations for undertaking tests in a ultra-weak gravitational field, where possible deviations from General Relativity can be tested [21]. Targeting the saddle point with high accuracy has become a major flight dynamic challenge.

Because LISA Pathfinder was proposed to conduct this experiment, the focus has been on finding low-Δv solutions, in the range of 1–2 m/s, which is relative to LISA Pathfinder end-of-life conditions. This stringent requirement justifies the high-fidelity model developed, although the Δv budget may be larger for dedicated SP missions, thus widening the design space [22]. Moreover, the specific option for LISA Pathfinder restricts the study to the actual spacecraft orbit, and

can be retrieved as a special case of the results presented. In essence, compared to previous works on the same subject [23–25], the present work features a higher degree of fidelity as well as a more sophisticated optimization scheme.

The paper is structured as follows. Section II is devoted to the derivation of the equations of motion with Lagrangian formalism and a mapping from inertial to roto-pulsating frame (RPF). The optimization techniques are described in Section III, whereas Section IV describes the results obtained for the selected case study. Section V summarizes the main outcomes and draws critical conclusions.

II. High-fidelity models

A. Inertial restricted n-body problem

A model for the description of the motion of a massless particle, P, subjected to the gravitational field of other $n-1$ celestial bodies P_j is the restricted n-body problem. We define the kinetic and potential energies per unit mass of P as

$$T = \frac{1}{2}\dot{\boldsymbol{R}}^\top \dot{\boldsymbol{R}}, \qquad V = -\sum_{j\in\mathcal{S}} \mu_j \left[\frac{1}{\|\boldsymbol{R}-\boldsymbol{R}_j\|} + \frac{J_{2_j} R_{B_j}^2}{2} \left(\frac{1}{\|\boldsymbol{R}-\boldsymbol{R}_j\|^3} - \frac{3(Z-Z_j)^2}{\|\boldsymbol{R}-\boldsymbol{R}_j\|^5} \right) \right], \tag{1}$$

where $\boldsymbol{R} = [X, Y, Z]^\top$ is the position of P in a solar barycentric inertial frame of reference, dots indicate time derivatives, $\mathcal{S}$ is the set containing P_j primaries characterized by μ_j gravitational parameter, $\boldsymbol{R}_j = [X_j, Y_j, Z_j]^\top$ position, R_{B_j} equatorial radius, and J_{2j} second harmonic coefficient related to inhomogeneous mass distribution. Accurate values for $\boldsymbol{R}_j(t)$, R_{B_j}, and J_{2j} are retrieved through the SPICE toolkit* [26, 27]. On top of the conservative terms in Eq. (1), a high-fidelity model also requires the inclusion of nonconservative forces. In this work, the effect of solar radiation pressure (SRP) is considered, which imparts a net acceleration to the spacecraft in the Sun-to-P direction equal to

$$\boldsymbol{a}_{SRP} = SP_0 \frac{\boldsymbol{R}-\boldsymbol{R}_s}{\|\boldsymbol{R}-\boldsymbol{R}_s\|^3}, \tag{2}$$

where SP_0 is the SRP parameter,

$$SP_0 = (1+c_r)\frac{A}{m}\frac{\Psi_0 d_0^2}{c}, \tag{3}$$

and c_r is the reflectivity coefficient of P, A/m its area to mass ratio, Ψ_0 the solar flux intensity at a distance d_0 from the Sun, c the speed of light, and $\boldsymbol{R}_s$ the Sun position. In Eq. (2), the cannonball model is assumed, for which the solar flux is inversely proportional to the square of the spacecraft distance from the Sun.

The equations of motion of P can be derived through a Lagrangian mechanics formalism, so yielding

$$\ddot{\boldsymbol{R}} + \nabla V = \boldsymbol{a}_{SRP}, \tag{4}$$

*The toolkit is freely available through the NASA NAIF website `http://naif.jpl.nasa.gov/naif/`. Last accessed on Oct. 11 2017.

where

$$\nabla V = \sum_{j\in\mathcal{S}} \mu_j \left[\frac{\boldsymbol{R}-\boldsymbol{R}_j}{\|\boldsymbol{R}-\boldsymbol{R}_j\|^3} + \frac{3}{2} J_{2_j} R_{B_j}^2 \left(\frac{I+2I_z}{\|\boldsymbol{R}-\boldsymbol{R}_j\|^5} - \frac{5I(\boldsymbol{R}-\boldsymbol{R}_j)^\top I_z(\boldsymbol{R}-\boldsymbol{R}_j)}{\|\boldsymbol{R}-\boldsymbol{R}_j\|^7} \right) (\boldsymbol{R}-\boldsymbol{R}_j) \right] \tag{5}$$

is the gradient of V, I is the 3-by-3 identity matrix, and I_z is a 3-by-3 null matrix except for the third diagonal component, which is 1.

B. Roto-pulsating restricted n-body problem

The equations of motion for P are now written in a form resembling that of the circular restricted three-body problem (CRTBP). To do so, a mapping from the inertial to a roto-pulsating frame (RPF) is needed [8]. In this frame, a pair of primaries, P_1 and P_2, are at rest on the x-axis (see Fig. 1). Let $\{t, \boldsymbol{R}, \boldsymbol{V}\}$ be the dimensional time, position, and velocity of P in the inertial frame, respectively, and let $\{\tau, \boldsymbol{\rho}, \boldsymbol{\eta}\}$ be their nondimensional counterparts in the RPF, respectively. (Note that $\boldsymbol{\eta} = \boldsymbol{\rho}' := \mathrm{d}\boldsymbol{\rho}/\mathrm{d}\tau$.) The transformation between the barycentric inertial frame and the RPF are [2]

$$\boldsymbol{R}(t) = \boldsymbol{b}(t) + k(t)C(t)\boldsymbol{\rho}(\tau), \tag{6a}$$

$$\boldsymbol{V}(t) = \dot{\boldsymbol{b}} + \dot{k}C\boldsymbol{\rho} + k\dot{C}\boldsymbol{\rho} + kC\dot{\tau}\boldsymbol{\eta}, \tag{6b}$$

$$\tau = \omega(t - t_0), \tag{6c}$$

where

$$\mathbf{b}(t) = \frac{m_1\mathbf{R}_1 + m_2\mathbf{R}_2}{m_1+m_2}, \qquad k(t) = \|\boldsymbol{R}_2 - \boldsymbol{R}_1\|, \qquad C(t) = [\mathbf{e}_1, \mathbf{e}_2, \mathbf{e}_3], \tag{7}$$

with

$$\mathbf{e}_1 = \frac{\boldsymbol{R}_2 - \boldsymbol{R}_1}{k}, \qquad \mathbf{e}_2 = \mathbf{e}_3 \times \mathbf{e}_1, \qquad \mathbf{e}_3 = \frac{(\boldsymbol{V}_2 - \boldsymbol{V}_1)\times(\boldsymbol{R}_2 - \boldsymbol{R}_1)}{\|(\boldsymbol{V}_2 - \boldsymbol{V}_1)\times(\boldsymbol{R}_2 - \boldsymbol{R}_1)\|}. \tag{8}$$

In Eqs. (7)–(8), m_i, $\boldsymbol{R}_i$, and $\boldsymbol{V}_i$ are the mass, position, and velocity of the selected primaries P_i, respectively, $i = 1, 2$. The coordinates transformation, Eq. (6a), is composed of three parts: 1) A translation of the origin from the solar system barycenter to the primaries center of mass, $\mathbf{b}(t)$; 2) A nondimensionalization through the scaling factor $k(t)$, which is the actual distance between the primaries; and 3) A rotation by means of the orthogonal cosine angle matrix, $C(t)$. It is easy to verify that in the RPF P_1 and P_2 have a constant distance and are always aligned with the x-axis, their position being $\boldsymbol{\rho}_1 = [-\mu, 0, 0]^\top$ and $\boldsymbol{\rho}_2 = [1-\mu, 0, 0]^\top$, respectively, and $\boldsymbol{\eta}_1 = \boldsymbol{\eta}_2 = 0$; $\mu = m_2/(m_1+m_2)$ is the mass parameter of the P_1–P_2 system. As a result, the new frame rotates and pulsates in a nonuniform fashion. The time transformation, Eq. (6c), shifts the initial epoch to t_0 and scales the time unit by means of the primaries mean motion about their common barycenter, ω. By choosing a constant mean motion, the average primaries revolution period is 2π, and $\dot{\tau} = \omega$.

The equations of motion for the roto-pulsating restricted n-body problem (RPRnBP) are thus derived by substituting

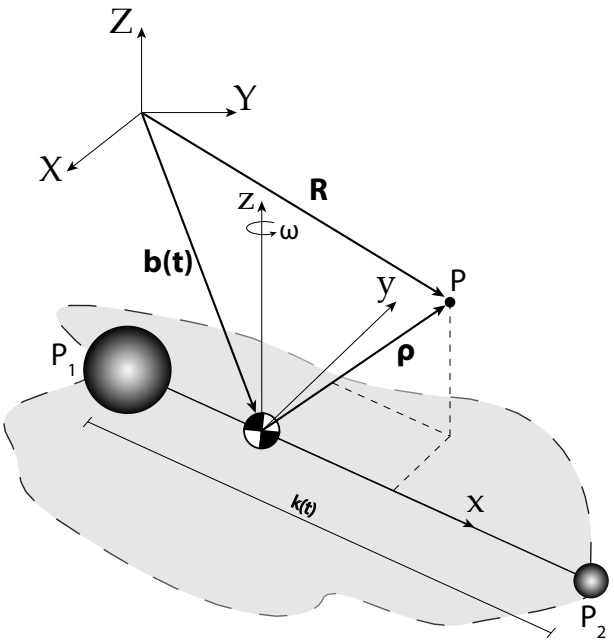

Fig. 1 Inertial frame (X, Y, Z) **and roto-pulsating frame** (x, y, z)**.**

Eqs. (6) into Eqs. (4)–(5). After some manipulations [2],

$$\boldsymbol{\rho}'' + \frac{1}{\omega}\left(\frac{2\dot{k}}{k}I + 2C^{\top}\dot{C}\right)\boldsymbol{\rho}' + \frac{1}{\omega^2}\left(\frac{\ddot{k}}{k}I + 2\frac{\dot{k}}{k}C^{\top}\dot{C} + C^{\top}\ddot{C}\right)\boldsymbol{\rho} + \frac{C^{\top}\ddot{\boldsymbol{b}}}{k\omega^2} = \nabla\Omega + \frac{SP_0}{\omega^2 k^3}\frac{\boldsymbol{\delta}_s}{\delta_s^3}, \tag{9}$$

where $\boldsymbol{\rho}_s$ is the Sun position in the RPF, $\boldsymbol{\delta}_s = \boldsymbol{\rho} - \boldsymbol{\rho}_s$, $\delta_s = \|\boldsymbol{\delta}_s\|$, and $\nabla\Omega = \partial\Omega/\partial\boldsymbol{\rho}$ is the gradient of the pseudo-potential

$$\Omega = \sum_{j\in\mathcal{S}} \frac{\hat{\mu}_j}{\delta_j}\left[1 + \frac{J_{2_j}R_{B_j}^2}{2k^2\delta_j^2}\left(1 - \frac{3\boldsymbol{\delta}_j^{\top}M\boldsymbol{\delta}_j}{\delta_j^2}\right)\right], \tag{10}$$

that is the equivalent of V in Eq. (1) transformed into nondimensional coordinates: $M = C^{\top}I_zC$, $\hat{\mu}_j = m_j/(m_1 + m_2)$, $\boldsymbol{\delta}_j = \boldsymbol{\rho} - \boldsymbol{\rho}_j$, and δ_j its magnitude. To derive Eq. (9), the relation $(\mu_1 + \mu_2)/(\omega^2 k^3) = 1$ is used. Mixed derivative notation in Eq. (9) acknowledge that ephemeris data is numeric, discrete, and provided for regular dimensional time.

C. Variational equation

Let $\boldsymbol{x} = [\boldsymbol{\rho}, \boldsymbol{\eta}]$ be the state vector of P in the RPRnBP. Then, the state space representation of Eq. (9) is

$$\boldsymbol{x}' = \boldsymbol{f}(\boldsymbol{x}, \tau) := \begin{bmatrix} \boldsymbol{f}_{\rho} \\ \boldsymbol{f}_{\eta} \end{bmatrix} \tag{11}$$

where $\boldsymbol{f}_\rho := \boldsymbol{\eta}$ and

$$\boldsymbol{f}_\eta(\boldsymbol{\rho}, \boldsymbol{\eta}, \tau) := \nabla\Omega - \frac{1}{\omega}\left(\frac{2\dot{k}}{k}I + 2C^\top\dot{C}\right)\boldsymbol{\eta} - \frac{1}{\omega^2}\left(\frac{\ddot{k}}{k}I + 2\frac{\dot{k}}{k}C^\top\dot{C} + C^\top\ddot{C}\right)\boldsymbol{\rho} - \frac{C^\top\ddot{\boldsymbol{b}}}{k\omega^2} + \frac{SP_0}{\omega^2 k^3}\frac{\boldsymbol{\delta}_s}{\delta_s^3}. \tag{12}$$

Let $\boldsymbol{x}(\tau) = \boldsymbol{\varphi}(\boldsymbol{x}_0, \tau_0; \tau)$ be the solution of Eq. (11) at time τ starting from $(\boldsymbol{x}_0, \tau_0)$. The state transition matrix (STM) of Eq. (11), that is, $\Phi(\tau_0, \tau) := \mathrm{d}\boldsymbol{\varphi}/\mathrm{d}\boldsymbol{x}_0$, is obtained by integrating the variational equation

$$\dot{\Phi}(\tau_0, \tau) = \left[\frac{\partial \boldsymbol{f}}{\partial \boldsymbol{x}}\right]\Phi(\tau_0, \tau), \qquad \Phi(\tau_0, \tau_0) = I_{6\times 6}. \tag{13}$$

Eq. (13) is equivalent to 36 first-order differential equations for the elements of Φ; it requires the terms in $[\partial \boldsymbol{f}/\partial \boldsymbol{x}]$ to be evaluated along the solution $\boldsymbol{x}(\tau)$, and therefore Eqs. (11) and (13) are to be integrated simultaneously, thus yielding a system of 42 first-order equations. With the expression of $\boldsymbol{f}$ given in Eq. (11), the Jacobian $[\partial \boldsymbol{f}/\partial \boldsymbol{x}]$ in Eq. (13) is

$$\left[\frac{\partial \boldsymbol{f}}{\partial \boldsymbol{x}}\right] := \begin{bmatrix} \mathbf{0} & I \\ \dfrac{\partial \boldsymbol{f}_\eta}{\partial \boldsymbol{\rho}} & \dfrac{\partial \boldsymbol{f}_\eta}{\partial \boldsymbol{\eta}} \end{bmatrix}, \tag{14}$$

where

$$\begin{aligned} \frac{\partial \boldsymbol{f}_\eta}{\partial \boldsymbol{\rho}} = &-\frac{1}{\omega^2}\left(\frac{\ddot{k}}{k}I + 2\frac{\dot{k}}{k}C^\top\dot{C} + C^\top\ddot{C}\right) - \sum_{j\in S}\hat{\mu}_j\left\{\frac{I}{\delta_j^3} - \frac{3\boldsymbol{\delta}_j\boldsymbol{\delta}_j^\top}{\delta_j^5} + \frac{3J_{2_j}R_{B_j}^2}{2k^2}\left[\frac{I + 2M}{\delta_j^5} - \right.\right. \\ &\left.\left.\frac{(5I + 10M)\boldsymbol{\delta}_j\boldsymbol{\delta}_j^\top + 5\boldsymbol{\delta}_j^\top M\boldsymbol{\delta}_j I + 10\boldsymbol{\delta}_j\boldsymbol{\delta}_j^\top M}{\delta_j^7} + 35\boldsymbol{\delta}_j^\top M\boldsymbol{\delta}_j\frac{\boldsymbol{\delta}_j\boldsymbol{\delta}_j^\top}{\delta_j^9}\right]\right\} + \frac{SP_0}{\omega^2 k^3}\left[\frac{I}{\delta_s^3} - \frac{3\boldsymbol{\delta}_s\boldsymbol{\delta}_s^\top}{\delta_s^5}\right], \end{aligned} \tag{15}$$

and

$$\frac{\partial \boldsymbol{f}_\eta}{\partial \boldsymbol{\eta}} = -\frac{2}{\omega}\left(\frac{\dot{k}}{k}I + C^\top\dot{C}\right). \tag{16}$$

In this work, Eq. (11) and (13) are integrated with a $7^{\text{th}}/8^{\text{th}}$ order variable step Runge–Kutta–Fehlberg scheme implemented with a Matlab mex file, and absolute and relative error tolerances set to 2.5×10^{-14}. Emphasis is put on the heaviness of the right-hand side evaluation of these 42 differential equations.

III. Impulsive trajectory optimization

A. Multiple burns multiple shooting formulation

Let $\boldsymbol{\psi}_0(\boldsymbol{x}(\tau_0), \tau_0) = \mathbf{0}$ and $\boldsymbol{\psi}_f(\boldsymbol{x}(\tau_f), \tau_f) = \mathbf{0}$ be general expressions for boundary conditions at some (unknown) initial and final epochs, τ_0 and τ_f, respectively, to which the solution of Eq. (11), $\boldsymbol{x}(\tau)$, must obey. A number of impulsive maneuvers are employed to drive $\boldsymbol{x}(\tau)$ from $\boldsymbol{\psi}_0$ to $\boldsymbol{\psi}_f$ hypersurfaces. The maneuvers are assumed to instantaneously alter the spacecraft velocity. A direct multiple shooting technique is developed, which accommodates an arbitrary

number of these maneuvers. With this method, the optimization is transcribed into a nonlinear programming (NLP) problem and solved for a finite set of variables [28]. Referring to Fig. 2, we define an *arc* as the ballistic portion of the trajectory separated by maneuvers, and a *segment* as the portion of the trajectory separated by two consecutive nodes. With n number of maneuvers and m nodes, there are $n+1$ arcs and $m-1$ segments within each arc. It is convenient to recall the core of the direct multiple shooting method.

Let $\tau_0^{(j)}$ and $\tau_f^{(j)}$ be the initial and final time of j-th arc, respectively, $j = 1, \ldots, n+1$. The time interval $[\tau_0^{(j)}, \tau_f^{(j)}]$ is discretized by using m evenly spaced points $\tau_0^{(j)} = \tau_1^{(j)} < \tau_2^{(j)} < \cdots < \tau_m^{(j)} = \tau_f^{(j)}$ over which the solution is sampled, that is, $\boldsymbol{x}_k^{(j)} = \boldsymbol{x}(\tau_k^{(j)})$, $k = 1, \ldots, m$. (j is an index running across arcs, k across nodes within each arc.) Solution continuity must be guaranteed within the arc, despite its subdivision into segments. The problem is to determine $\boldsymbol{x}_k^{(j)}$ such that

$$\boldsymbol{\zeta}_k^{(j)} := \boldsymbol{\varphi}(\boldsymbol{x}_k^{(j)}, \tau_k^{(j)}; \tau_{k+1}^{(j)}) - \boldsymbol{x}_{k+1}^{(j)} = 0; \quad k = 1, \ldots, m-1, \quad j = 1, \ldots, n+1. \tag{17}$$

Eqs. (17) are completed by imposing time and position continuity at both endpoints of each *inner* arc

$$\boldsymbol{\psi}_j := \boldsymbol{\rho}_m^{(j)} - \boldsymbol{\rho}_1^{(j+1)} = \mathbf{0}, \quad \sigma_j := \tau_m^{(j)} - \tau_1^{(j+1)} = 0, \quad j = 1, \ldots, n; \tag{18}$$

and by enforcing boundary conditions $\boldsymbol{\psi}_0(\boldsymbol{x}_1^{(1)}, \tau_1^{(1)}) = \mathbf{0}$ and $\boldsymbol{\psi}_f(\boldsymbol{x}_m^{(n+1)}, \tau_m^{(n+1)}) = \mathbf{0}$ at the beginning of the first arc and the end of the last arc, respectively. While $\boldsymbol{\psi}_j = \mathbf{0}$ guarantee continuity of positions, a discontinuous velocity arises between two adjacent arcs, namely

$$\Delta\boldsymbol{\eta}_j := \boldsymbol{\eta}_m^{(j)} - \boldsymbol{\eta}_1^{(j+1)}, \qquad j = 1, \ldots, n. \tag{19}$$

Note that Eq. (17) and Eqs. (18)–(19) represent nonlinear and linear equality constraints to the problem, respectively.

A schematic representation of the overall multiple burn multiple shooting method is shown in Fig. 2. Notice that the interface between two arcs, j and $j+1$, features two nodes, $\boldsymbol{x}_m^{(j)}$ and $\boldsymbol{x}_1^{(j+1)}$, belonging to the previous and next arc,

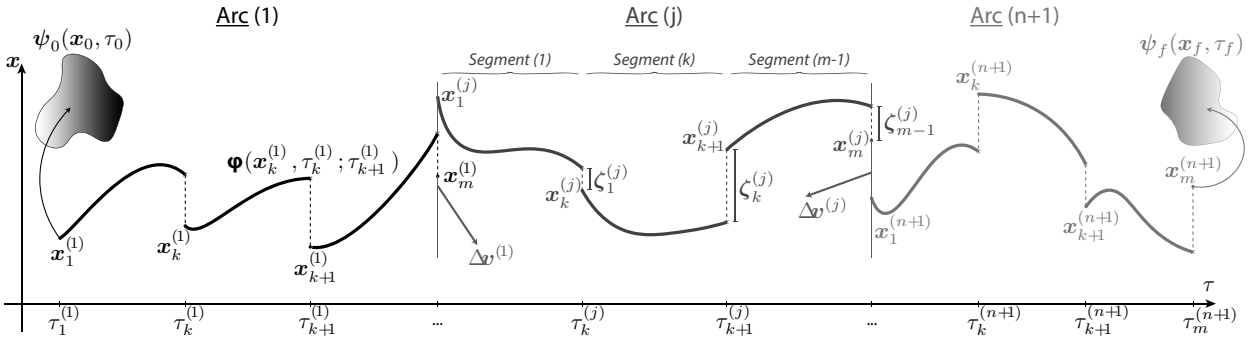

Fig. 2 Multiple burns, multiple shooting strategy.

respectively. This choice reduces the interdependence among arcs to obtain a better structured Jacobian matrix (see Section III.C) at the cost of increasing the number of variables.

B. Statement of the optimization problem

For each arc, the optimization variables are made of the collection of states at the nodes, $\boldsymbol{x}_k^{(j)}$, as well as the initial and final time, $\tau_1^{(j)}$ and $\tau_m^{(j)}$. Therefore, the overall $(6m+2)\times(n+1)$-dimensional NLP variable column vector is

$$\boldsymbol{y} = \left(\boldsymbol{x}_k^{(j)},\ \tau_1^{(j)},\ \tau_m^{(j)}\right), \quad k = 1,\dots,m, \quad j = 1,\dots,n+1 \tag{20}$$

The NLP variables embed hence the initial and final times of each arc, which are allowed to vary. The aim is to minimize the sum of impulses, Δv_j, which are related to the propellant consumed. The objective function is thus

$$J(\boldsymbol{y}) := \sum_{j=1}^{n} (\Delta v_j)^2 = \omega^2 \sum_{j=1}^{n} \| k(\tau_m^{(j)})\boldsymbol{\eta}_m^{(j)} - k(\tau_1^{(j+1)})\boldsymbol{\eta}_1^{(j+1)} \|^2. \tag{21}$$

The time-dependence of J in Eq. (21) is stressed: given $\|\Delta\boldsymbol{\eta}_j\|$ (nondimensional), the magnitude of Δv_j (dimensional) depends upon *when* the maneuver is executed through $k(\tau)$, this being the length unit (see Eq. (6a)).

The impulsive trajectory optimization is to solve the NLP problem

$$\min_{\boldsymbol{y}} J(\boldsymbol{y}) \quad \text{s.t.} \quad \boldsymbol{g}(\boldsymbol{y}) = \boldsymbol{0} \quad \text{and} \quad \boldsymbol{h}(\boldsymbol{y}) \le \boldsymbol{0}, \tag{22}$$

where $\boldsymbol{g}$ and $\boldsymbol{h}$ are vector-valued functions stating equality and inequality constraints, respectively. The former read

$$\boldsymbol{g}(\boldsymbol{y}) := \left(\boldsymbol{\zeta}_k^{(p)}, \boldsymbol{\psi}_j,\ \sigma_j,\ \boldsymbol{\psi}_0,\ \boldsymbol{\psi}_f\right), \quad k = 1,\dots,m-1, \quad j = 1,\dots,n, \quad p = 1,\dots,n+1, \tag{23}$$

where the last two entries enforce respect of boundary conditions. The inequality constraints are instead

$$\boldsymbol{h}(\boldsymbol{y}) := \left(\omega \sum_{j=1}^{n} k(\tau_m^{(j)}) \|\Delta\boldsymbol{\eta}^{(j)}\| - \Delta v_{\max},\ \tau_m^{(n+1)} - \tau_1^{(1)} - \Delta\tau_{\max},\ \tau_1^{(p)} - \tau_m^{(p)} + \Delta\tau_{\min}^{(p)}\right), \quad p = 1,\dots,n+1, \tag{24}$$

which enforce the respect of (i) an upper limit for the Δv budget, $\omega \sum_j k(\tau_m^{(j)})\|\Delta\boldsymbol{\eta}_j\| \le \Delta v_{\max}$; (ii) a maximum transfer duration, $\tau_m^{(n+1)} - \tau_1^{(1)} \le \Delta\tau_{\max}$; and (iii) a minimum arc duration, $\tau_m^{(p)} - \tau_1^{(p)} \ge \Delta\tau_{\min}^{(p)}$, where $\Delta\tau_{\min}^{(p)} = \max\{\bar{\Delta\tau}_{\min}, m\omega k(\tau_m^{(p)})\|\Delta\boldsymbol{\eta}_p\|/T_{\max}\}$, for $p = 1,\dots,n$, and $\Delta\tau_{\min}^{(p)} = \bar{\Delta\tau}_{\min}$ for $p = n+1$. In the latter, the maneuver feasibility is considered through a conservative overestimation of the duration that is necessary to spread the impulsive maneuver Δv_j into an equivalent finite-thrust arc for a probe of mass m thrusting at maximum thrust, $T_{\max}$ [29].

C. Accurate computation of Jacobian of defect constraints

Providing accurate and fast information on the objective function and constraints derivatives with respect to the NLP variables is of paramount importance for the multiple shooting numerical efficiency and convergence performances. In the present analysis, the objective function and constraints possess simple derivative expressions, with the exception of the Jacobian of defect constraints (Eq. (17)). To avoid using finite difference methods, these derivatives are extracted from the STM, which in turn is computed by integrating the variational equations described in Eq. (13). The use of information contained in the STM not only allows an increased accuracy in the derivatives computation (on the order of the numerical propagator tolerance), but also an increased robustness of the algorithm itself [30].

The focus is on computing the derivative of $\boldsymbol{\varphi}(\boldsymbol{x}_k, \tau_k; \tau_{k+1})$ in Eq. (17) with respect to $\boldsymbol{x}_k$, τ_k, and τ_{k+1} (superscripts are dropped to ease notation). An analytical result is used to link the derivative of the flow with its STM [14, 31]:

$$\frac{\mathrm{d}\boldsymbol{\varphi}}{\mathrm{d}\boldsymbol{x}_k} = \Phi(\tau_k, \tau_{k+1}), \qquad \frac{\mathrm{d}\boldsymbol{\varphi}}{\mathrm{d}\tau_k} = -\Phi(\tau_k, \tau_{k+1})\boldsymbol{f}(\boldsymbol{x}_k, \tau_k), \qquad \frac{\mathrm{d}\boldsymbol{\varphi}}{\mathrm{d}\tau_{k+1}} = \boldsymbol{f}(\boldsymbol{\varphi}(\boldsymbol{x}_k, \tau_k; \tau_{k+1}), \tau_{k+1}), \tag{25}$$

where $\boldsymbol{f}$ is the vector field in Eq. (11). While the first and last relations in Eq. (25) are straightforward and directly stem from the definition of STM and flow, respectively, the second equation is not trivial and deserves a dedicated treatment.

Remark 1 (Initial Flow Projection). Let $\boldsymbol{\varphi}(\boldsymbol{x}_0, \tau_0; \tau)$ be the flow at τ of a general dynamics $\dot{\boldsymbol{x}} = \boldsymbol{f}(\boldsymbol{x}, \tau)$, with $\boldsymbol{f} : \mathbb{R}^{n+1} \to \mathbb{R}^n$, starting from initial conditions $(\boldsymbol{x}_0, \tau_0)$. A change in the sole initial value of the independent variable, τ_0, affects the flow at τ proportionally to the system state transition matrix from τ_0 to τ and vector field at $(\boldsymbol{x}_0, \tau_0)$, i. e.,

$$\frac{\mathrm{d}\boldsymbol{\varphi}}{\mathrm{d}\tau_0} = -\Phi(\tau_0, \tau)\, \boldsymbol{f}(\boldsymbol{x}_0, \tau_0). \tag{26}$$

The proof of Remark 1 is given in the Appendix. Referring to Fig. 2 and assuming a uniform time discretization within each arc, with segment duration $\Delta\tau = (\tau_m - \tau_1)/(m-1)$, we have

$$\tau_k = \tau_1 + (k-1)\frac{\tau_m - \tau_1}{m-1}, \quad k = 1, \ldots, m. \tag{27}$$

Since the NLP variables for each arc are $\{\boldsymbol{x}_k\}_{k=1}^m$, τ_1, and τ_m, the derivatives of $\boldsymbol{\zeta}_k$ in Eq. (17) with respect to these quantities have to be calculated. By virtue of Remark 1, and using the results in Eqs. (25), these derivatives read

$$\begin{aligned}
&\frac{\mathrm{d}\boldsymbol{\zeta}_k}{\mathrm{d}\boldsymbol{x}_k} = \Phi(\tau_k, \tau_{k+1}), \qquad \frac{\mathrm{d}\boldsymbol{\zeta}_k}{\mathrm{d}\boldsymbol{x}_{k+1}} = -I_{6\times 6}, \qquad k = 1, \ldots, m-1, \\
&\frac{\mathrm{d}\boldsymbol{\zeta}_k}{\mathrm{d}\tau_1} := \frac{\mathrm{d}\tau_k}{\mathrm{d}\tau_1}\frac{\mathrm{d}\boldsymbol{\varphi}}{\mathrm{d}\tau_k} + \frac{\mathrm{d}\tau_{k+1}}{\mathrm{d}\tau_1}\frac{\mathrm{d}\boldsymbol{\varphi}}{\mathrm{d}\tau_{k+1}} = -\frac{m-k}{m-1}\Phi(\tau_k, \tau_{k+1})\boldsymbol{f}(\boldsymbol{x}_k, \tau_k) + \frac{m-k-1}{m-1}\boldsymbol{f}(\boldsymbol{\varphi}(\boldsymbol{x}_k, \tau_k, \tau_{k+1}), \tau_{k+1}), \\
&\frac{\mathrm{d}\boldsymbol{\zeta}_k}{\mathrm{d}\tau_m} := \frac{\mathrm{d}\tau_k}{\mathrm{d}\tau_m}\frac{\mathrm{d}\boldsymbol{\varphi}}{\mathrm{d}\tau_k} + \frac{\mathrm{d}\tau_{k+1}}{\mathrm{d}\tau_m}\frac{\mathrm{d}\boldsymbol{\varphi}}{\mathrm{d}\tau_{k+1}} = -\frac{k-1}{m-1}\Phi(\tau_k, \tau_{k+1})\boldsymbol{f}(\boldsymbol{x}_k, \tau_k) + \frac{k}{m-1}\boldsymbol{f}(\boldsymbol{\varphi}(\boldsymbol{x}_k, \tau_k, \tau_{k+1}), \tau_{k+1}).
\end{aligned} \tag{28}$$

In Fig. 3 the structure of Jacobian for nonlinear equality constraints is reported for $m = 6$, $n = 2$ (5 segments, 3 arcs). The terms across the diagonal block are those given by $\mathrm{d}\boldsymbol{\zeta}_k/\mathrm{d}\boldsymbol{x}_k$ and $\mathrm{d}\boldsymbol{\zeta}_k/\mathrm{d}\boldsymbol{x}_{k+1}$, whereas the columns in the rightmost part of the matrix represent $\mathrm{d}\boldsymbol{\zeta}_k/\mathrm{d}\tau_1$ and $\mathrm{d}\boldsymbol{\zeta}_k/\mathrm{d}\tau_m$ for the three arcs. The bottom part of the Jacobian is made of $\mathrm{d}\boldsymbol{\psi}_0/\mathrm{d}\boldsymbol{x}_0$, $\mathrm{d}\boldsymbol{\psi}_f/\mathrm{d}\boldsymbol{x}_f$, and $\mathrm{d}\boldsymbol{\psi}_f/\mathrm{d}\tau_f$. Note that the derivatives of the linear equality constraints in Eq. (23) ($\boldsymbol{\psi}_j$ and σ_j) are not reported for simplicity. In Fig. 3, it can be seen how the choice of repeating the node at arcs interfaces produces an arc-wise structured Jacobian, which can be constructed recursively once m and n are given.

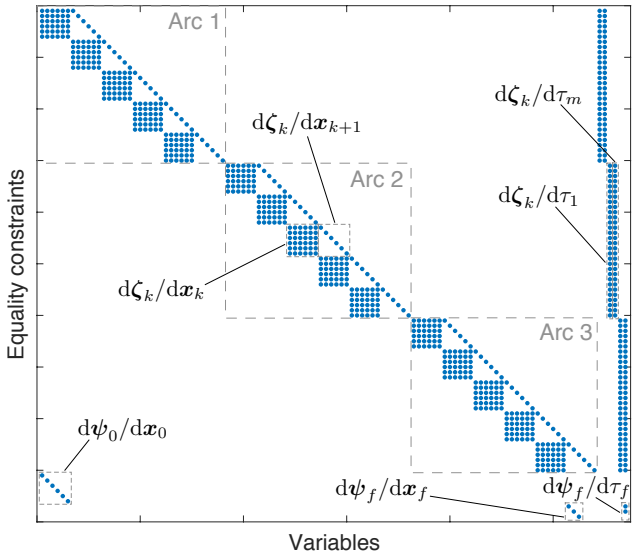

Fig. 3 Structure of Jacobian for nonlinear equality constraints.

IV. Case study: Optimal transfers to the Sun–Earth saddle point

Evidence is mounting about the importance of the gravitational SP within the solar system [23]. Regions about the SP present clean, close-to-zero background acceleration environments where possible tests of the General Relativity can be conducted. In particular, Modified Newtonian Dynamics (MOND) and Tensor-Vector-Scalar (TeVeS) can be valid alternative gravity theories when accelerations are below 10^{-10} m/s^2 [21, 24, 32]. Among the SP in the solar system, the Sun–Earth one seems particularly appealing due to its relatively easy accessibility [24, 25, 33]: it is located at a distance of approximately 258, 800 km from the Earth, along the Sun–Earth line, between the Sun and the Earth. Although saddle points seem to be remarkable locations in the solar system, they are still unexplored.

In this work, the multiple burns multiple shooting algorithm presented in Section III is applied to find trajectories that pass through the Sun–Earth saddle point. A miss distance of up to 50 km is tolerated, while no requirement for the relative velocity at the saddle point is set. In view of a mission extension scenario (e.g., LISA Pathfinder), our analysis focuses on spacecraft already orbiting about Sun–Earth $L_{1,2}$ halos. Thus, optimal halo-to-SP transfers in the Sun–Earth system are sought. Table 1 gives the physical parameters used in the analysis below..

Table 1 Parameters of the Sun–Earth–Moon system and the spacecraft.

Parameter	Symbol	Value
Sun–Earth mass ratio	μ	$3.003480593992993 \times 10^{-6}$
Earth gravitational parameter	μ_3	398600.4354360959 km^3/s^2
Moon gravitational parameter	μ_{10}	4902.800066163796 km^3/s^2
Length unit	LU	$1.495978706136889 \times 10^8$ km
Time unit	TU	58.13235351684487 days
Velocity unit	VU	29.78473657194809 km/s
Earth mean radius	R_{B_3}	6371.008366666666 km
Moon mean radius	$R_{B_{10}}$	1737.4 km
Earth oblateness coefficient	J_{2_3}	0.001082616
Moon oblateness coefficient	$J_{2_{10}}$	0
SRP parameter	SP_0	$2.210656810849369 \times 10^6$ km^3/s^2
L_1 location w.r.t. Earth	x_{L_1}	$-1.491551005309341 \times 10^6$ km
L_2 location w.r.t. Earth	x_{L_2}	$1.501531764462003 \times 10^6$ km
Reflectivity coefficient	c_r	0.08
Area-to-mass ratio	A/m	0.02 m^2/kg
Sun–Earth saddle point in the CRTBP	$\hat{x}_{\text{SP}}$	258, 813.23 km or 0.998266936932953

A. Location of the Sun–Earth saddle point

By definition, the gravitational saddle point is the location in the configuration space where the net gravitational accelerations balance. It is a fixed point just in the CRTBP, located at $\hat{x}_{\text{SP}}$ (see Table 1). In a higher-fidelity model, the SP position, $\boldsymbol{R}_{\text{SP}}$, is calculated by solving Newton's gravitational law

$$\sum_{j \in \mathcal{S}} \hat{\mu}_j \frac{\boldsymbol{R}_j - \boldsymbol{R}_{\text{SP}}}{\|\boldsymbol{R}_j - \boldsymbol{R}_{\text{SP}}\|^3} = \boldsymbol{0}, \tag{29}$$

once the ephemerides of the celestial bodies in $\mathcal{S}$ are known. Eq. (6a) is applied to $\boldsymbol{R}_{\text{SP}}$, solution of Eq. (29), to obtain the saddle point trajectory in the RPRnBP. The SP trajectory shown in Fig. 4 is computed for 1, 500 days starting on December 3 2015 04:47:27.928 TDB (LISA Pathfinder launch epoch).

B. Importance of high-fidelity modeling

Table 2 shows the Sun–Earth SP position shift with respect to its fixed position in the Sun–Earth circular restricted three body problem for each celestial body considered. The lunar gravity causes the largest perturbation, followed by Jupiter and Venus. Because in some applications the minimum saddle point distance for a meaningful measurement can be in the order of 1 km [23], the saddle point location knowledge should be determined at sub-km precision.

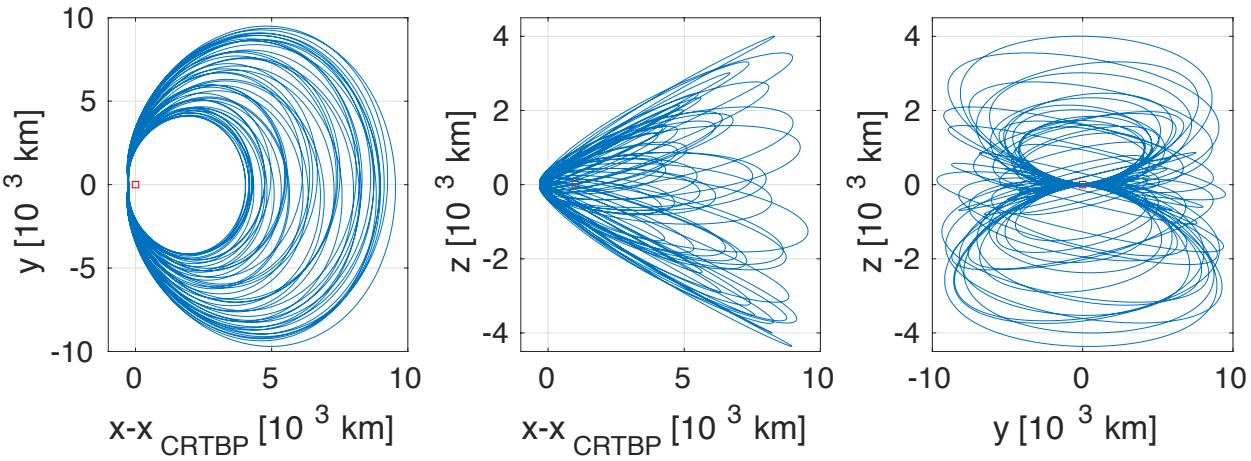

Fig. 4 Sun–Earth saddle point trajectory in the RPRnBP.

This requirement imposes accounting for all the celestial bodies in Table 2. Moreover, the perturbation due to Earth oblateness is necessary in view of the numerous close encounters experienced in optimal LPO-to-SP transfers (see Section IV.D). A quantitative analysis on the accelerations due to the solar radiation pressure shows values in the order of 10^{-7} m/s^2, which is comparable to the perturbation by Jupiter, and is only one order of magnitude smaller than the thrust-to-mass ratio of a 1000-kg spacecraft equipped with a 1-mN thruster. The importance of the perturbing actions for the specific application case motivates the high-fidelity model developed.

C. Departure leg and boundary conditions

It is assumed that the spacecraft initially lies on the unstable manifold of a halo orbit about either L_1 or L_2 of the Sun–Earth system. The displacement along the unstable direction is 150 km in position and 3 cm/s in velocity [34]. Accordingly, the initial state is specified by using 1) the halo out-of-plane amplitude, $A_z \in [5, 50] \times 10^4$ km; 2) the nondimensional time along the halo, t_{po}, spanning a complete period; and 3) an initial epoch, t_0, through which the states of all retained celestial bodies are determined. The initial epoch spans a duration of 29 days, from March 30 to April 28, 2017. This time interval is sufficient for a complete lunar revolution around the Earth and is able to capture the largest perturbative effects on the spacecraft orbit toward the saddle point. The considered halo out-of-plane interval encloses the one of LISA Pathfinder, roughly retracing an $A_z = 40 \times 10^4$ km amplitude halo.

Table 2 Shift of Sun–Earth saddle point location in meters.

	Moon	Jupiter	Venus	Saturn	Mars	Mercury	Uranus	Neptune
Min	241.09×10^3	2.93×10^3	104.33	291.90	5.92	10.02	12.83	6.79
Max	11200.75×10^3	10.33×10^3	4.34×10^3	777.57	324.50	72.31	30.07	15.72
Mean	2055.87×10^3	6.86×10^3	732.50	572.66	68.14	28.26	22.00	11.48

A thorough exploration of the search space is performed in [22]. Initial guesses correspond to orbits intercepting a bubble of 10,000 km centered at the saddle point within 5 years. A total of 942/578 solutions departing from L_1/L_2 are processed by the multiple burns multiple shooting algorithm. The timing, direction, and magnitude of impulsive maneuvers are optimized to target the saddle point (see [22] for more details on the first guess generation).

D. Results

Optimal transfers to the saddle point have been calculated for $n = 5$, $m = 3$. These values are primarily suggested by numerical simulations and convergence rate analysis of the multiple shooting algorithm in simpler models. The number of NLP variables is thus 120. Table 3 displays the algorithm performances in terms of converged solutions ratio. The number of converged solutions is higher for L_1-departing transfers. One third of L_2 initial conditions provide optimal transfers to the SP, thus highlighting the difficulty and the larger cost necessary to reach the SP from the L_2 LPO region for the solutions samples studied in this work. This result meets the expectations of the search space exploration in [22].

Figs. 5–6 illustrate a few examples of transfer trajectories starting from L_1 (Fig. 5) and L_2 (Fig. 6) halo unstable manifolds. Transfers have been labeled according to geometrical features to aid interpretation and to group the solutions into families. The implementation of the optimization is able to deal with a wide variety of solutions, from short/direct transfers to longer ones, characterized by multiple chaotic revolutions and close passages about Earth and/or Moon. The multiple burns multiple shooting algorithm implemented here scans the solution space and finds optimal transfers with quite different parameters. This diversity aids a more robust mission analysis.

Fig. 7 shows the time of flight and total Δv cost for optimal L_1 (see Fig. 7a) and L_2 (see Fig. 7b). The solutions are grouped according to the initial halo amplitude into three sets: dark dots for $A_z \in [5, 15] \times 10^4$ km, shaded dots for $A_z \in (15, 30] \times 10^4$ km, and light colored dots for $A_z \in (30, 50] \times 10^4$ km. A sample LISA Pathfinder mission extension option is indicated in Fig. 7 (Δv = 1 m/s, ToF = 180 days); a richer solution set can be found in [12]. Interestingly, there are many solutions with short time of flight (ToF) to the Sun–Earth saddle point featuring also low Δv. This result suggests the possibility of successfully leveraging the highly nonlinear nature of the RPRnBP to reach the SP at moderate cost and duration [35]. The two quasi-vertical lines in Fig. 7a where many optimal solutions cluster, are the fast/direct σ_1 transfers shown in Figs. 5b–5c. The clustering of optimal short ToF solutions is less pronounced for L_2-departing orbits. In both $L_{1,2}$ transfers, smaller halos reach the SP at a lower cost and shorter ToF. This is conjectured to be driven

Table 3 Number of solutions for the $L_{1,2}$ cases.

Departure LPO	Initial guesses	Optimal solutions	Convergence rate
L_1	942	393	41.72%
L_2	578	191	33.04%

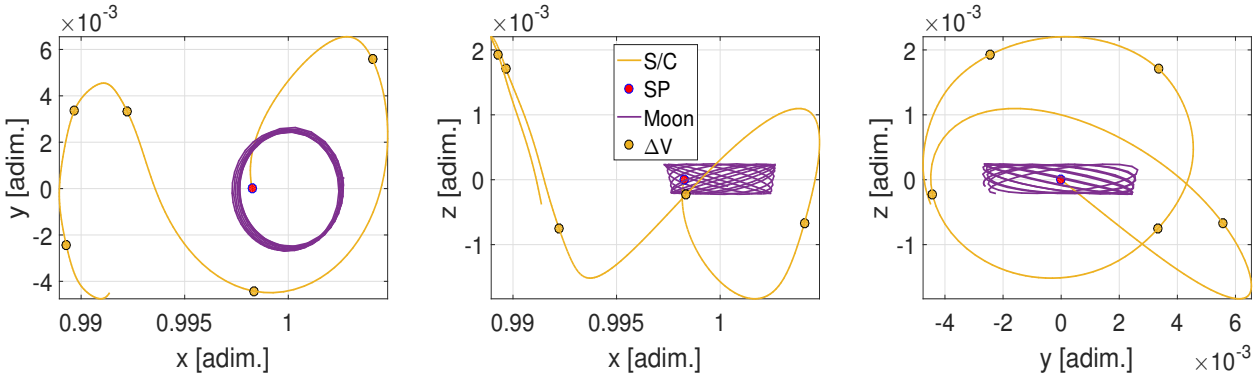

(a) δ_1 transfer (Δv = 0.991 m/s and ToF = 239.45 days).

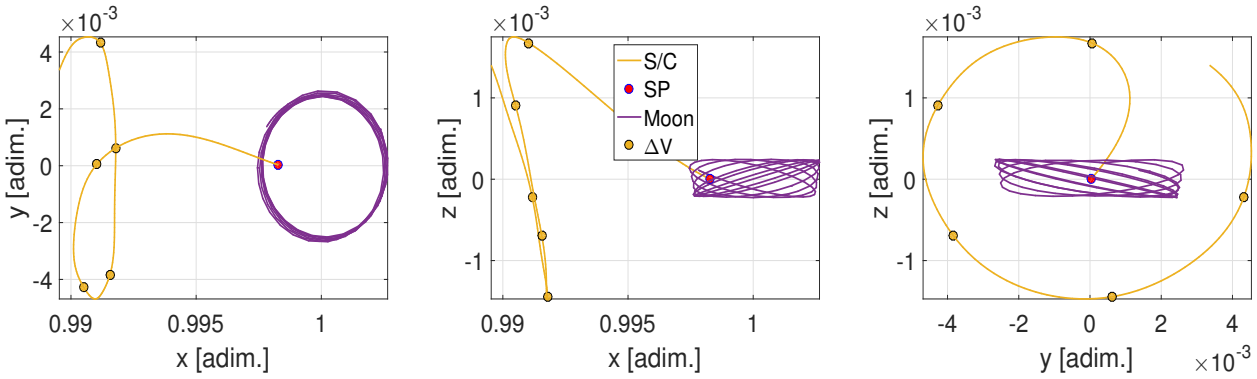

(b) σ_1 transfer (Δv = 0.260 m/s and ToF = 188.10 days).

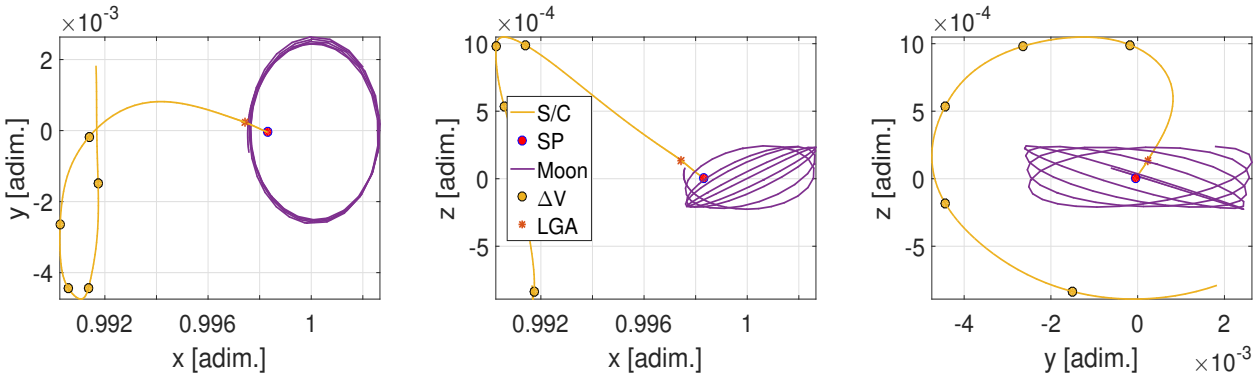

(c) σ_1 transfer with one Moon close passage (termed LGA) (Δv = 0.297 m/s and ToF = 172.72 days).

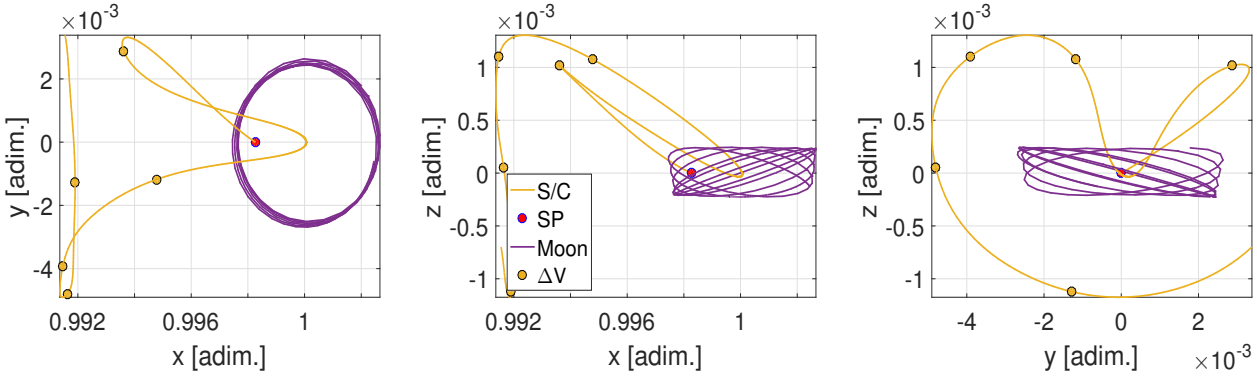

(d) g_1 transfer with one Earth close passage (Δv = 1.337 m/s and ToF = 129.89 days).

Fig. 5 Optimal transfer samples to the SP from L_1.

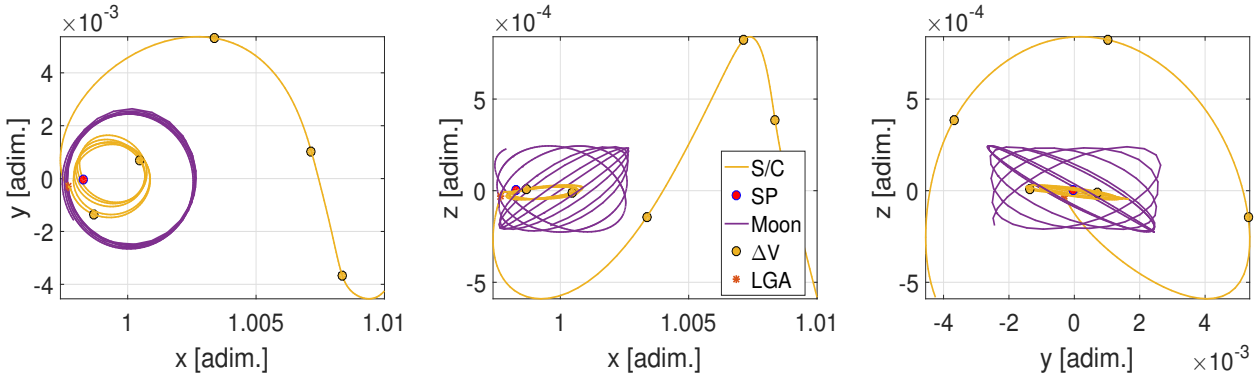

(a) δ_2 transfer with one Moon close passage (termed LGA) (Δv = 0.706 m/s and ToF = 173.26 days).

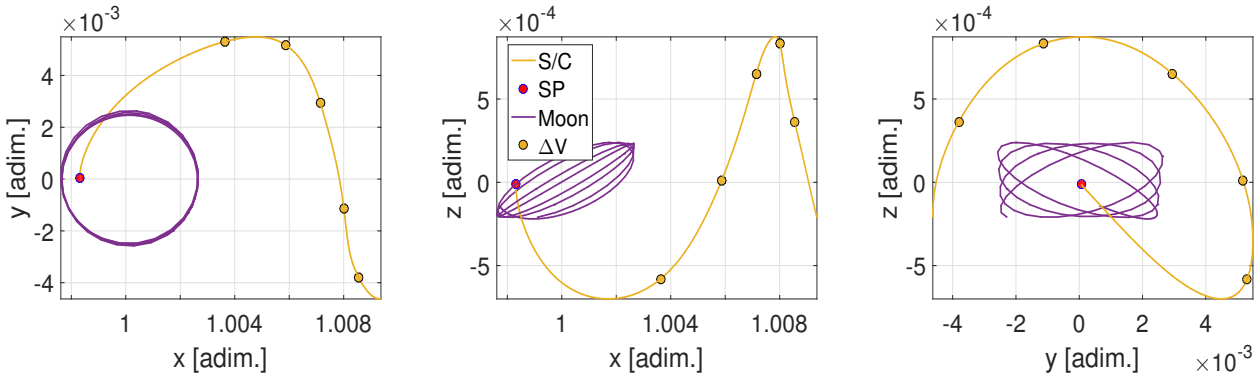

(b) σ_2 transfer (Δv = 1.261 m/s and ToF = 111.17 days).

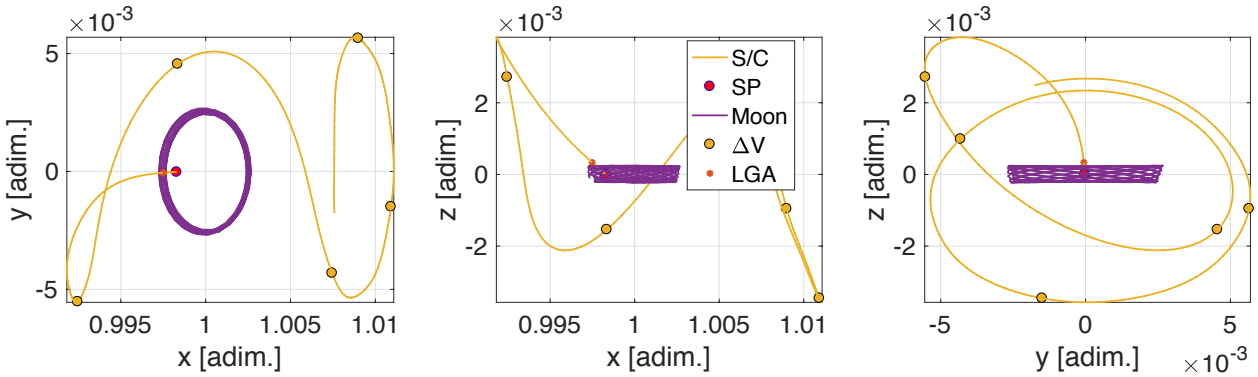

(c) Ω_2 transfer with one Moon close passage (termed LGA) (Δv = 1.617 m/s and ToF = 323.94 days).

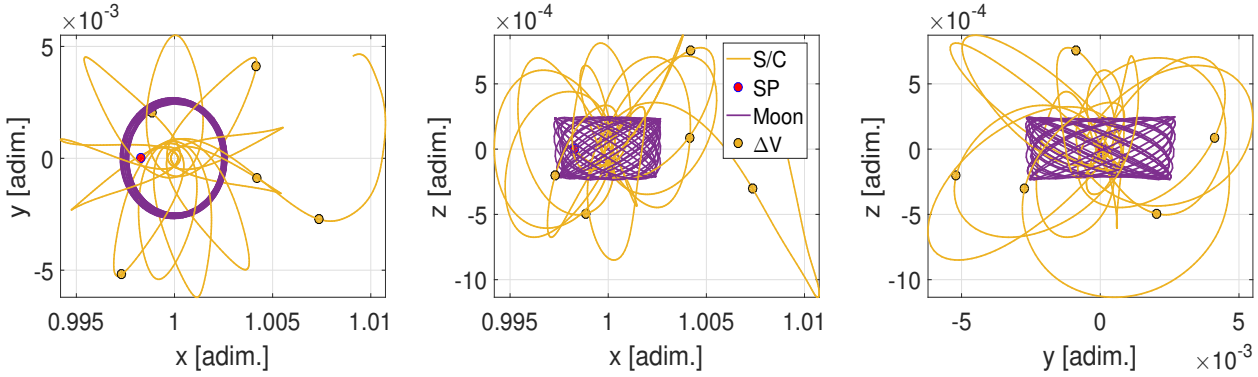

(d) Transfer with multiple Earth close passages (Δv = 0.720 m/s and ToF = 537.83 days).

Fig. 6 Examples of optimal transfers to the SP from L_2.

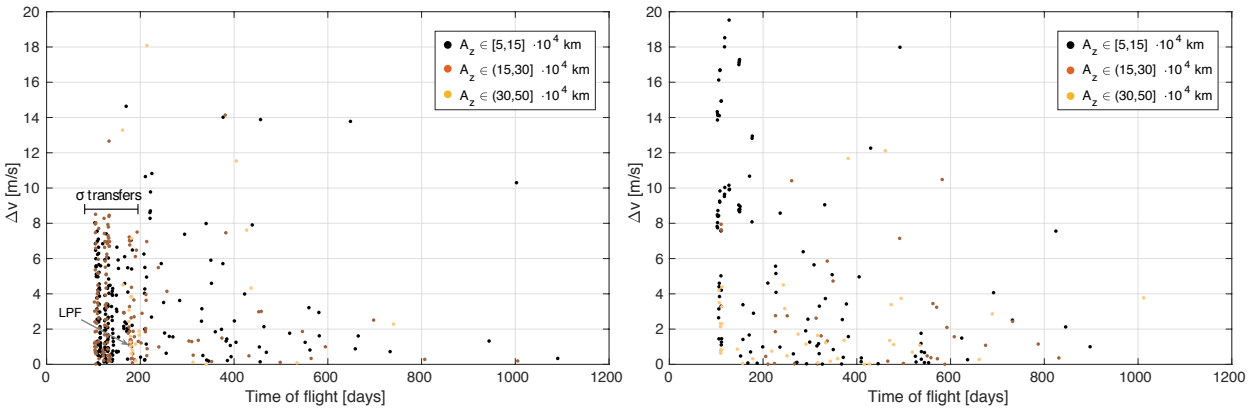

(a) L_1-departing transfers.

(b) L_2-departing transfers.

Fig. 7 Time of flight and total deterministic Δv cost for optimal halos-to-SP transfers in the RPRnBP.

by the geometry of the unstable manifolds emanating from smaller halos, when compared to those emanating from larger ones.

In view of the accurate position knowledge required at the saddle point, navigation and orbit determination errors play an important role both for the correct injection onto the halo unstable manifold and for the accurate execution of the impulsive maneuvers. A preliminary analysis estimates the navigation cost of the fast direct transfers in the order of 1 m/s with initial position and velocity knowledge typical of already-operative spacecraft [12]. The sum of design (deterministic) and navigation (stochastic) cost suggest feasibility of low-Δv transfers from Sun–Earth LPO to SP as viable mission extension of end-of-life spacecraft.

V. Conclusions

In this work, a direct multiple burns multiple shooting technique is applied to the Sun–Earth gravitational saddle point transfer problem. Efficient algorithmic procedures are implemented to solve a complex problem with a rich high-fidelity dynamics, where many fuel-optimal trajectories are sought from the Sun–Earth libration point orbits region to the saddle point. Results in the Sun–Earth–Moon system — 393/191 solutions departing from L_1/L_2 are found — indicate an abundance of options with a variety of characteristics, including low time of flight, low total Δv, and self-disposing nature. The case of LISA Pathfinder mission extension is included in the application scenario.

Targeting the Sun–Earth gravitational saddle point, for instance to test of General Relativity-related theories, is more cost-effective for L_1-departing transfers when compared to L_2 orbits. Due to the geometry of the problem and the effects of solar radiation pressure, L_2-departing transfers requires, on average, higher Δv and longer cruises to reach the saddle point. However, the total deterministic Δv is below 20 m/s for all presented transfers, a value well within the technological capabilities of spacecraft currently orbiting or scheduled to orbit in LPO regions.

Appendix: Proof of Remark 1

Proof. By definition,

$$\frac{\mathrm{d}\boldsymbol{\varphi}}{\mathrm{d}\tau_0} = \lim_{\delta\tau_0 \to 0} \frac{\boldsymbol{\varphi}(\boldsymbol{x}_0, \tau_0 + \delta\tau_0; \tau) - \boldsymbol{\varphi}(\boldsymbol{x}_0, \tau_0; \tau)}{\delta\tau_0}. \tag{30}$$

It can be noticed that

$$\boldsymbol{\varphi}(\boldsymbol{x}_0, \tau_0 + \delta\tau_0; \tau) = \boldsymbol{\varphi}(\boldsymbol{x}_0 + \delta\boldsymbol{x}_0, \tau_0; \tau), \tag{31}$$

which states that the solution triggered by an infinitesimal initial time shift, $\delta\tau_0$, is equivalent to the flow generated from the unperturbed initial time, τ_0, subject to an infinitesimal change in initial state, $\delta\boldsymbol{x}_0$. A time variation is thus translated into a variation of state, provided that the nominal and perturbed solutions are sufficiently close. A visual interpretation is provided in Fig. 8. By using the definition of STM, the right-hand side of Eq. (31) can be written up to the first order as

$$\boldsymbol{\varphi}(\boldsymbol{x}_0 + \delta\boldsymbol{x}_0, \tau_0; \tau) = \boldsymbol{\varphi}(\boldsymbol{x}_0, \tau_0; \tau) + \frac{\mathrm{d}\boldsymbol{\varphi}}{\mathrm{d}\boldsymbol{x}_0}\,\delta\boldsymbol{x}_0 = \boldsymbol{\varphi}(\boldsymbol{x}_0, \tau_0; \tau) + \Phi(\tau_0, \tau)\delta\boldsymbol{x}_0, \tag{32}$$

and substituting Eqs. (31)–(32) in Eq. (30) one gets

$$\frac{\mathrm{d}\boldsymbol{\varphi}}{\mathrm{d}\tau_0} = \Phi(\tau_0, \tau) \lim_{\delta\tau_0 \to 0} \frac{\delta\boldsymbol{x}_0}{\delta\tau_0}. \tag{33}$$

Note that Eqs. (31)–(33) hold valid as long as the displaced state $\boldsymbol{\varphi}(\boldsymbol{x}_0, \tau_0 + \delta\tau_0; \tau)$ remains in a neighborhood of $\boldsymbol{\varphi}(\boldsymbol{x}_0, \tau_0; \tau)$. Under the assumption of infinitesimal variations, $\boldsymbol{x}_0 = (\boldsymbol{x}_0 + \delta\boldsymbol{x}_0) + \delta\tau_0\, \boldsymbol{f}(\boldsymbol{x}_0, \tau_0)$ (Euler step), which yields $\delta\boldsymbol{x}_0 = -\boldsymbol{f}(\boldsymbol{x}_0, \tau_0)\,\delta\tau_0$. Substitution of the latter into Eq. (33) generates Eq. (26). □

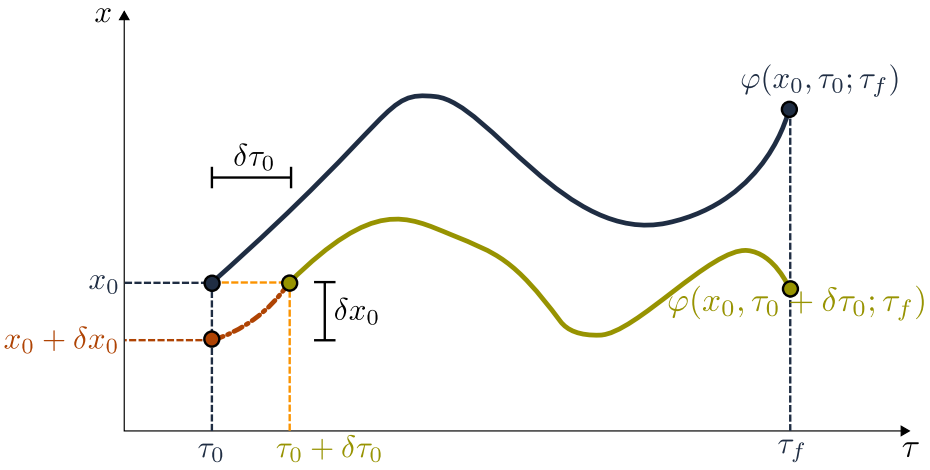

Fig. 8 Representation of the Initial Flow Projection (Remark 1).

Funding Sources

Part of the work presented in this paper has been conducted under European Space Agency Contract No. 4000118201/16/F/MOS "Feasibility of ultra low thrust transfers in L_1/L_2 Sun–Earth–Moon systems" (ESA ITT 8601).

Acknowledgments

The authors would like to acknowledge Dr. Florian Renk, Mirco Rasotto, and Erind Veruari for their support.

References

[1] Zanetti, R., Holt, G., Gay, R., D'Souza, C., Sud, J., Mamich, H., Begley, M., King, E., and Clark, F. D., "Absolute Navigation Performance of the Orion Exploration Flight Test 1," *Journal of Guidance, Control, and Dynamics*, Vol. 40, No. 5, 2017, pp. 1106–1116. doi:10.2514/1.G002371.

[2] Dei Tos, D. A., and Topputo, F., "Trajectory refinement of three-body orbits in the real solar system model," *Advances in Space Research*, Vol. 59, No. 8, 2017, pp. 2117–2132. doi:10.1016/j.asr.2017.01.039.

[3] Howell, K. C., and Pernicka, H. J., "Numerical determination of Lissajous trajectories in the restricted three-body problem," *Celestial mechanics*, Vol. 41, No. 1, 1987, pp. 107–124. doi:10.1007/BF01238756.

[4] Dei Tos, D. A., Russell, R., and Topputo, F., "Survey of Mars ballistic capture trajectories using periodic orbits as generating mechanisms," *Journal of Guidance, Control, and Dynamics*, Vol. accessed May 14, 2018, 2018, pp. 1–16. doi:10.2514/1.G003158.

[5] Topputo, F., "On optimal two-impulse Earth–Moon transfers in a four-body model," *Celestial Mechanics and Dynamical Astronomy*, Vol. 117, No. 3, 2013, pp. 279–313. doi:10.1007/s10569-013-9513-8.

[6] Belbruno, E., and Miller, J. K., "Sun-perturbed Earth-to-Moon transfers with ballistic capture," *Journal of Guidance, Control, and Dynamics*, Vol. 16, No. 4, 1993, pp. 770–775. doi:10.2514/3.21079.

[7] Topputo, F., and Belbruno, E., "Earth–Mars transfers with ballistic capture," *Celestial Mechanics and Dynamical Astronomy*, Vol. 121, No. 4, 2015, pp. 329–346. doi:10.1007/s10569-015-9605-8.

[8] Gómez, G., Masdemont, J. J., and Mondelo, J. M., "Solar system models with a selected set of frequencies," *Astronomy and Astrophysics*, Vol. 390, No. 2, 2002, pp. 733–750. doi:10.1051/0004-6361:20020625.

[9] Dei Tos, D. A., and Topputo, F., "On the advantages of exploiting the hierarchical structure of astrodynamical models," *Acta Astronautica*, Vol. 136, 2017, pp. 236–247. doi:10.1016/j.actaastro.2017.02.025.

[10] Amato, D., Baù, G., and Bombardelli, C., "Accurate orbit propagation in the presence of planetary close encounters," *Monthly Notices of the Royal Astronomical Society*, Vol. 470, No. 2, 2017, pp. 2079–2099. doi:10.1093/mnras/stx1254.

[11] Arora, N., and Russell, R. P., "A fast, accurate, and smooth planetary ephemeris retrieval system," *Celestial Mechanics and Dynamical Astronomy*, Vol. 108, No. 2, 2010, pp. 107–124. doi:10.1007/s10569-010-9296-0.

[12] Topputo, F., Dei Tos, D. A., Rasotto, M., and Renk, F., "Design and Feasibility Assessment of Ultra Low Thrust Trajectories to the Sun–Earth Saddle Point," *Space Flight Mechanics Meeting, AIAA SciTech Forum, (AIAA 2018–1691)*, American Institute of Aeronautics and Astronautics, 2018, pp. 1–15. doi:10.2514/6.2018-1691.

[13] Kemble, S., *Interplanetary mission analysis and design*, Springer Science & Business Media, 2006.

[14] Marchand, B. G., Howell, K. C., and Wilson, R. S., "Improved Corrections Process for Constrained Trajectory Design in the n-Body Problem," *Journal of Spacecraft and Rockets*, Vol. 44, No. 4, 2007, pp. 884–897. doi:10.2514/1.27205.

[15] Pavlak, T. A., and Howell, K., "Evolution of the out-of-plane amplitude for quasi-periodic trajectories in the Earth–Moon system," *Acta Astronautica*, Vol. 81, No. 2, 2012, pp. 456–465. doi:10.1016/j.actaastro.2012.07.025.

[16] Alessi, E. M., Gómez, G., and Masdemont, J. J., "A Methodology for the Computation of Constrained Orbits and its Application to the Design of Solar System Trajectories," *The Journal of the Astronautical Sciences*, Vol. 59, No. 3, 2012, pp. 477–501. doi:10.1007/s40295-014-0004-2.

[17] Ozimek, M. T., and Howell, K. C., "Low-Thrust Transfers in the Earth-Moon System, Including Applications to Libration Point Orbits," *Journal of Guidance, Control, and Dynamics*, Vol. 33, No. 2, 2010, pp. 533–549. doi:10.2514/1.43179.

[18] Zuiani, F., Vasile, M., Palmas, A., and Avanzini, G., "Direct transcription of low-thrust trajectories with finite trajectory elements," *Acta Astronautica*, Vol. 72, 2012, pp. 108–120. doi:10.1016/j.actaastro.2011.09.011.

[19] Elnagar, G., Kazemi, M. A., and Razzaghi, M., "The pseudospectral Legendre method for discretizing optimal control problems," *IEEE Transactions on Automatic Control*, Vol. 40, No. 10, 1995, pp. 1793–1796. doi:10.1109/9.467672.

[20] Fahroo, F., and Ross, I. M., "Direct Trajectory Optimization by a Chebyshev Pseudospectral Method," *Journal of Guidance, Control, and Dynamics*, Vol. 25, No. 1, 2002, pp. 160–166. doi:10.2514/2.4862.

[21] Milgrom, M., "A modification of the Newtonian dynamics as a possible alternative to the hidden mass hypothesis," *Astrophysical Journal*, Vol. 270, 1983, pp. 365–370. doi:10.1086/161130.

[22] Topputo, F., Dei Tos, D. A., Rasotto, M., and Nakamiya, M., "The Sun–Earth saddle point: characterization and opportunities to test general relativity," *Celestial Mechanics and Dynamical Astronomy*, Vol. 130, No. 4, 2018, p. 33. doi:10.1007/s10569-018-9824-x.

[23] Trenkel, C., Kemble, S., Bevis, N., and Magueijo, J., "Testing Modified Newtonian Dynamics with LISA Pathfinder," *Advances in Space Research*, Vol. 50, No. 11, 2012, pp. 1570–1580. doi:10.1016/j.asr.2012.07.024.

[24] Fabacher, E., Kemble, S., Trenkel, C., and Dunbar, N., "Multiple Sun–Earth Saddle Point flybys for LISA Pathfinder," *Advances in Space Research*, Vol. 52, No. 1, 2013, pp. 105–116. doi:10.1016/j.asr.2013.02.005.

[25] Cox, A., and Howell, K. C., "Transfers to a Sun–Earth Saddle Point: An Extended Mission Design Option for LISA Pathfinder," *Advances in the Astronautical Sciences*, Vol. 158, No. I, 2016, pp. 653–668.

[26] Acton Jr, C. H., "Ancillary data services of NASA's navigation and ancillary information facility," *Planetary and Space Science*, Vol. 44, No. 1, 1996, pp. 65–70. doi:10.1016/0032-0633(95)00107-7.

[27] Acton Jr, C. H., Bachman, N., Semenov, B., and Wright, E., "A look towards the future in the handling of space science mission geometry," *Planetary and Space Science*, Vol. 150, 2018, pp. 9–12. doi:10.1016/j.pss.2017.02.013.

[28] Betts, J. T., "Survey of Numerical Methods for Trajectory Optimization," *Journal of Guidance, Control, and Dynamics*, Vol. 21, No. 2, 1998, pp. 193–207. doi:10.2514/2.4231.

[29] Ocampo, C. A., and Mathur, R., "Variational Model for Optimization of Finite-Burn Escape Trajectories Using a Direct Method," *Journal of Guidance, Control and Dynamics*, Vol. 35, No. 2, 2012, pp. 598–608. doi:10.2514/1.52606.

[30] Pellegrini, E., and Russell, R. P., "On the Computation and Accuracy of Trajectory State Transition Matrices," *Journal of Guidance, Control, and Dynamics*, Vol. 39, No. 11, 2016, pp. 2485–2499. doi:10.2514/1.G001920.

[31] Whitley, R. J., and Ocampo, C. A., "Direct multiple shooting optimization with variable problem parameters," *47th AIAA Aerospace Sciences Meeting including The New Horizons Forum and Aerospace Exposition, Aerospace Sciences Meetings*, American Institute of Aeronautics and Astronautics, 2009, pp. 1–16. doi:10.2514/6.2009-803.

[32] Trenkel, C., and Kemble, S., "Gravitational science with LISA Pathfinder," *Journal of Physics: Conference Series*, Vol. 154, No. 1, 2009, p. 012002. doi:10.1088/1742-6596/154/1/012002.

[33] Bekenstein, J. D., and Magueijo, J., "Modified Newtonian dynamics habitats within the solar system," *Physical Review D*, Vol. 73, 2006, pp. 103513.1–14. doi:10.1103/PhysRevD.73.103513.

[34] Topputo, F., "Fast numerical approximation of invariant manifolds in the circular restricted three-body problem," *Communications in Nonlinear Science and Numerical Simulation*, Vol. 32, No. Supplement C, 2016, pp. 89–98. doi:10.1016/j.cnsns.2015.08.004.

[35] Dei Tos, D. A., "Trajectory optimization of limited control authority spacecraft in high-fidelity models," Ph.D. thesis, Politecnico di Milano, 2018. doi:10.13140/RG.2.2.15099.00804, URL `http://hdl.handle.net/10589/137086`.